One Earth

Minimizing uncertainties in climate projections and water budget reveals the vulnerability of freshwater to climate change

Highlights

- The multivariate technique corrects GCM biases and closes the water budget better

- Soil drainable porosities determine WS surplus or deficit and runoff relationships

- Land use types and climate change enhance WS deficit or surplus

- Additional moisture intake into basins does not always initiate surplus WS

Authors

Oluwafemi E. Adeyeri, Wen Zhou,
Christopher E. Ndehedehe,
Xuan Wang, Kazeem A. Ishola,
Patrick Laux

Correspondence

wen_zhou@fudan.edu.cn (W.Z.)

In brief

Food security and human sustainability are at risk due to rising water needs, especially in areas where resources are scarce. This work advances the knowledge of terrestrial water storage (WS) changes in a warming world by assessing the WS patterns using observations and climate experiments. The results show that different factors impact moisture movements in and out of basins. Climate change and land use type are major drivers in the observed trends and characteristics of WS surpluses or deficits.

CellPress

Article

Minimizing uncertainties in climate projections and water budget reveals the vulnerability of freshwater to climate change

Oluwafemi E. Adeyeri,[1,2,5] Wen Zhou,[2,3,9,*] Christopher E. Ndehedehe,[4,5] Xuan Wang,[1] Kazeem A. Ishola,[6,7] and Patrick Laux[8]

[1]Low-Carbon and Climate Impact Research Centre, School of Energy and Environment, City University of Hong Kong, Kowloon 999077, Hong Kong SAR
[2]Key Laboratory of Polar Atmosphere-Ocean-Ice System for Weather and Climate, Ministry of Education and Department of Atmospheric and Oceanic Sciences and Institute of Atmospheric Sciences, Fudan University, Shanghai 200433, China
[3]Key Laboratory for Polar Science of the MNR, Polar Research Institute of China, Shanghai, China
[4]School of Environment and Science, Griffth University, Nathan, QLD 4111, Australia
[5]Australian Rivers Institute, Griffith University, Nathan, QLD 4111, Australia
[6]Irish Climate Analysis and Research Units (ICARUS), Department of Geography, Maynooth University, Maynooth W23 VP22, Ireland
[7]National Centre for Geocomputation, Maynooth University, Maynooth W23 F2H6, Ireland
[8]Institute for Meteorology and Climate Research, Atmospheric Environmental Research, Karlsruhe Institute of Technology, Campus Alpine, 82467 Garmisch-Partenkirchen, Germany
[9]Lead contact
*Correspondence: oeadeyeri2-c@my.cityu.edu.hk (O.E.A.), wen_zhou@fudan.edu.cn (W.Z.)
https://doi.org/10.1016/j.oneear.2023.12.013

SCIENCE FOR SOCIETY Rising global temperatures will increase water in the atmosphere and diminish terrestrial water resources. Understanding changes in stored terrestrial water in surface or underground reservoirs is crucial for ecosystem and human sustainability. For example, modern agriculture often depends on groundwater and reservoirs, and water storage changes affect crop yield. Climate change will alter how much water is stored terrestrially; therefore, predicting these changes is crucial for adapting crops and other human water needs to changing water resources. Our findings reveal that warmer temperatures and shifting precipitation patterns can increase plant water consumption and evapotranspiration and reduce stored water. Stored water also depends on land use. For example, converting natural wetlands into urban areas reduces groundwater. The implications of warmer climates on water storage are region dependent, potentially exacerbating competition for water between human and natural ecosystems.

SUMMARY

Global water scarcity threatens agriculture, food security, and human sustainability. Hence, understanding changes in terrestrial water storage (WS) is crucial. By utilizing climate models, reanalysis, and satellite data, we demonstrate the effectiveness of the multivariate bias correction technique in facilitating precise WS representation while ensuring robust water budget closure. Historical data indicate seasonal changes, where forested basins exhibit a WS surplus in the December-January-February season, with a reversal in the June-July-August-September season. Non-forested basins display varied patterns influenced by geographical location and land use type. Future projections indicate increased June-July-August-September deficits in most Southern Hemisphere basins under the middle-road (SSP 245) scenario and wetter December-January-February conditions under the regional rivalry (SSP 370) scenario. Weather and climate systems governing WS vary by season and basin, resulting in inconsistent moisture intake into basins. These findings underscore the intricate interplay between moisture transport, land characteristics, and the resulting WS, highlighting the need to understand these complex interactions for effective regional water resource management strategies in changing climates.

INTRODUCTION

Terrestrial water storage, hereafter called water storage (WS), is the ability of the environment to maintain an efficient water resource system through the interception, infiltration, and storage of precipitation through the canopy, litter, soil, and lake reservoir water bodies in space and time.[1,2] WS boosts base flow in the dry season, normalizes the uneven temporal distribution of runoff, and reduces peak flooding in flood season.[3] This multifaceted process ensures the availability of water resources critical for sustaining agricultural activities, securing food availability, and supporting various ecosystems. This has profound implications for both human and environmental systems. Beyond its ecological impact, WS plays a pivotal role in human livelihoods, influencing water supply sustainability and public well-being. A WS deficit—i.e., the shortfall between the amount of water stored in various terrestrial reservoirs (such as groundwater, soil moisture, and surface water) and the expected levels for a given area or time frame—often occurs when there is an imbalance in the water cycle due to factors like prolonged drought, reduced precipitation, increased evaporation, or excessive water extraction. This may result in severe water shortages, food insecurity, habitat degradation, species extinction, unsustainable water supply sources, and heightened public tension.[4,5]

Climate change significantly alters the global hydrological cycle and its various WS components. The anticipated shifts in precipitation patterns, intensities, and temperature regimes due to climate change are expected to profoundly impact WS dynamics. Because climate change modifies the global hydrological cycle, the distribution, amount, and timing of WS components such as runoff, precipitation, and evapotranspiration will likely undergo significant changes.[6–8] For example, increased evapotranspiration leads to a decrease in soil moisture in summer and more snowfall accumulation in wetter winters that melts early in warm springs, thereby altering the runoff regime.[9,10] These meteorological factors, combined with land use land cover (LULC) dynamics,[6] ecology factors, soil attributes, and topography, contribute to the complexities of WS dynamics, especially across space, time, and various domains.[11] Such alterations directly affect human systems, influencing water availability for agriculture, industry, and domestic use. Moreover, shifts in WS can impact extreme weather events, contributing to challenges such as floods or droughts that can disrupt communities and economies. Nevertheless, the efficacy of proactive planning and adaptation strategies to mitigate potential WS risks to human and environmental systems critically relies on precise investigations and WS projections in a changing climate.

Long-term datasets are imperative for understanding the overarching patterns of WS dynamics, encompassing seasonal variations and potential shifts over the years. While direct observations provide a substantial amount of valuable information, the availability of such data is often restricted due to various factors, including limited accessibility, inadequate monitoring infrastructure, and financial constraints. To cushion some constraints, satellite data, particularly from the Gravity Recovery and Climate Experiment (GRACE) mission,[12] pioneered the measurement of large-scale changes in WS after 2002. Underpinned by model-derived outputs, assessing WS components using GRACE data on a basin/regional to continental scale is now feasible.[13–15]

GRACE data have been widely used in WS assessments such as flood and drought monitoring, global freshwater availability, ocean dynamics, and water budget closure analysis.[16–18] Despite these applications, the temporal coverage of the data (2002–present) remains a notable limitation in WS impact assessment. This duration is insufficient for comprehensive monitoring of long-term changes in WS patterns, particularly when assessing changes attributed to climate variation over extended periods—typically over 30-year intervals. Consequently, the constraints associated with observational and satellite data hinder the accurate monitoring and evaluation of long-term shifts in WS dynamics.

WS dynamics have been widely monitored using the water budget model to understand long-term changes in WS, particularly at a basin scale. A water budget model is a conceptual framework that accounts for WS within a defined system. The main components of the water budget model include precipitation, evapotranspiration, runoff, and changes in storage. Precipitation represents water input into the system, while evapotranspiration accounts for the water returned to the atmosphere through processes such as plant transpiration and soil and water evaporation. Runoff encompasses the water that flows over the land surface, eventually contributing to rivers and lakes. Changes in storage consider alterations in soil moisture, groundwater levels, and other reservoirs within the system. In essence, WS is one of the critical components of the hydrological cycle, often derived from the water budget model that describes the balance between precipitation, evapotranspiration, and runoff. The spatiotemporal evolution of WS can also be inferred from the summation of soil moisture, snow cover, and groundwater.[19]

Several studies[20–22] have described the hydro-climatic variations in river basins by evaluating various components of the hydrological cycle,[9,20,23–25] demonstrating that precipitation plays a crucial role in driving WS in tropical, hot semi-arid, and temperate climates with dry winters.[2,26] In specific locations in the mid and high latitudes without dry seasons, evapotranspiration becomes a primary driver of WS changes. In contrast, temperature dominates in cold-arid regions with dry summers.[2] However, it is crucial to note that individual water budget components interact and influence WS dynamics differently across various scales.[1,8,9,23,27] For example, hydro-climatic factors are not the sole mechanisms driving WS behavior; climate change-induced glacial retreat and human activities, including water consumption and changes in LULC, have also been identified as significant driving forces behind WS changes.[28] Evidence indicates that an increase in forest cover is associated with a decrease in river discharge.[27,29] Increased deforestation and urbanization have also been associated with high land surface temperature and thermal stress[6,30,31] and unpredictable river discharge peak dynamics.[27] Increased WS losses are also directly attributed to human activities, particularly unsustainable groundwater abstraction in global drylands and warming-induced glacier loss in humid regions.[28,32] Because of the intricate interplay among various hydro-climatic factors, comprehending the fundamental hydro-meteorological processes influenced by large-scale atmospheric processes, LULC, and their complex feedback interactions presents considerable challenges. Furthermore, the intricate nature of WS, coupled with uncertainties and the nonlinear hydro-meteorological processes involved in assessing individual water budget components, restricts the practical application of

the water budget approach in impact assessment due to the water budget closure problem.

Numerical and climate models have been developed to overcome these complexities and to enhance our understanding of the Earth's complex, nonlinear hydro-meteorological processes. These models also help address the emerging water budget closure problem arising from using different sources of datasets to balance the water budget.[16] Climate models provide efficient synopses in exploring water budget components (i.e., precipitation, runoff, evapotranspiration, and WS changes), which are challenging to monitor thoroughly on a global scale. However, general circulation models are unsuitable for impact research due to their poor resolution (inability to capture fine-scale details effectively) and their inadequate depiction of microphysical processes[33–36] due to oversimplification of real-world features, which jointly magnify the inherent biases in global circulation models.[33,34] Therefore, correcting these biases and investigating how well various correction strategies can mimic the signs of climate change[33,37] are crucial. While bias correction (BC) methods have been widely employed to correct global circulation models meteorological variables, there remains uncertainty regarding their performance in correcting WS and how they address the water budget closure problem. Furthermore, the uncertainties linked to individual water budget components while estimating WS with the water budget approach limit their applicability in impact assessment. For example, evapotranspiration, a water budget component calculated using the water budget equation, accords well with estimates from remote sensing regarding the seasonal cycle but demonstrates more inter-annual variability and more significant magnitudes.[24,25,38,39] In essence, inferring WS as a residual of other water components, without proper evaluation, could produce erroneous results due to inherent uncertainties associated with each component, lack of closure in the water budget model, and other drivers of WS change (e.g., LULC). Hence, the need to provide a critical understanding of the projected changes in WS characteristics and the roles of large-scale atmospheric processes and LULC using a synergy of climate model outputs, reanalysis dataset, and remote sensing observations is imperative and requires further attention in the context of a changing climate. Also, addressing the uncertainties and biases from different driving WS datasets is required to achieve accurate water budget closure.[16,40,41]

Here, we investigate changes in WS by evaluating two BC techniques that aim to improve the representation of WS changes while reducing uncertainties in the water budget closure within the Coupled Model Intercomparison Project Phase 6 (CMIP6) global climate models (GCMs), reanalysis dataset and remote sensing observations. The improved representation of WS has significant implications for water resource management, ecological conservation, and climate change adaptation strategies. We observe that the multivariate BC approach improves WS representation and closes the water budget reasonably. This improvement offers a more precise representation of global terrestrial water changes within the CMIP6 GCMs for historical data and future projections. Hence, we utilize the information from multivariate BC outputs to achieve the following:

(1) assess global WS changes to enhance our understanding of WS trends, projections, and seasonal characteristics under different climate change scenarios, including the middle of the road (SSP 245), regional rivalry (SSP 370), and fossil-fueled development (SSP 585) scenarios and

(2) explore the potential influences of LULC, global wind systems, and water vapor transport on WS changes.

By investigating the intricate relationships among various factors, we establish that land use and land cover patterns, alongside moisture transport into and out of basins—regulated by global wind and pressure systems—exert significant influence on global terrestrial water changes.

RESULTS AND DISCUSSION

Method summary

We investigate long-term WS dynamics derived from the water budget equation and GRACE data. However, using univariate and multivariate BC approaches, we aimed to improve WS representation while reducing uncertainties in water budget closure within CMIP6 GCMs, reanalysis dataset, and remote sensing observations. The univariate quantile mapping BC strategy maps the source distribution quantiles to target distribution quantiles. In contrast, the multivariate BC techniques[33,42–44] consider the whole multivariate dependency structures between several dependent and independent climate variables.[33,42,45] The multivariate dependency structure shows the connections between each independent variable (e.g., precipitation and runoff) and each dependent variable (e.g., WS). Thus, the multivariate approach consistently corrects biases across multiple variables,[33,42–44] while the univariate method corrects each variable (e.g., evapotranspiration) independently. We conduct a comprehensive assessment of the accuracy of each GCM and BC method, employing various performance statistics. Our investigation includes estimating trends and examining the joint dependency structures among water budget variables. We employ self-organizing maps[31,46] and Gaussian mixture models[31] to enhance our understanding of classifying WS into surpluses and deficits. Additionally, we analyze the dynamics and trends of WS, considering the influence of different LULCs, large-scale climate events, and climate change scenarios.

Performance of BC methods and GCMs

Assessing the long-term average state of CMIP6 WS from 1959 to 2014 using the spatial root-mean-square error (RMSE) reveals discrepancies in the performance of different GCMs across various regions. For example, in the Amazon basin, the CMCC (Centro Euro-Mediterraneo sui Cambiamenti Climatici Earth System Model 2) model exhibits an RMSE ranging from 10 to over 140 mm, while the UKESM (United Kingdom Earth System Modelling project (Low Resolution)) model ranges from 0 to 100 mm (Figures S1A–S1J). The higher RMSE observed in the CMCC model, surpassing 140 mm in many tropical regions and highland areas like the Himalayas, indicates substantial deviations from the reference data. These deviations may be attributed to variations in land surface schemes, misrepresentation of vegetation and orography, unrealistic large-scale variability, and divergent internal variability between climate models and observations.[33–35,47] Figure S1K validates the uncertainty from using varied water budget component datasets for estimating WS.[16,40] The uncertainties range from 0 to 120 mm RMSE, especially in the tropics and mid-latitudes. Higher
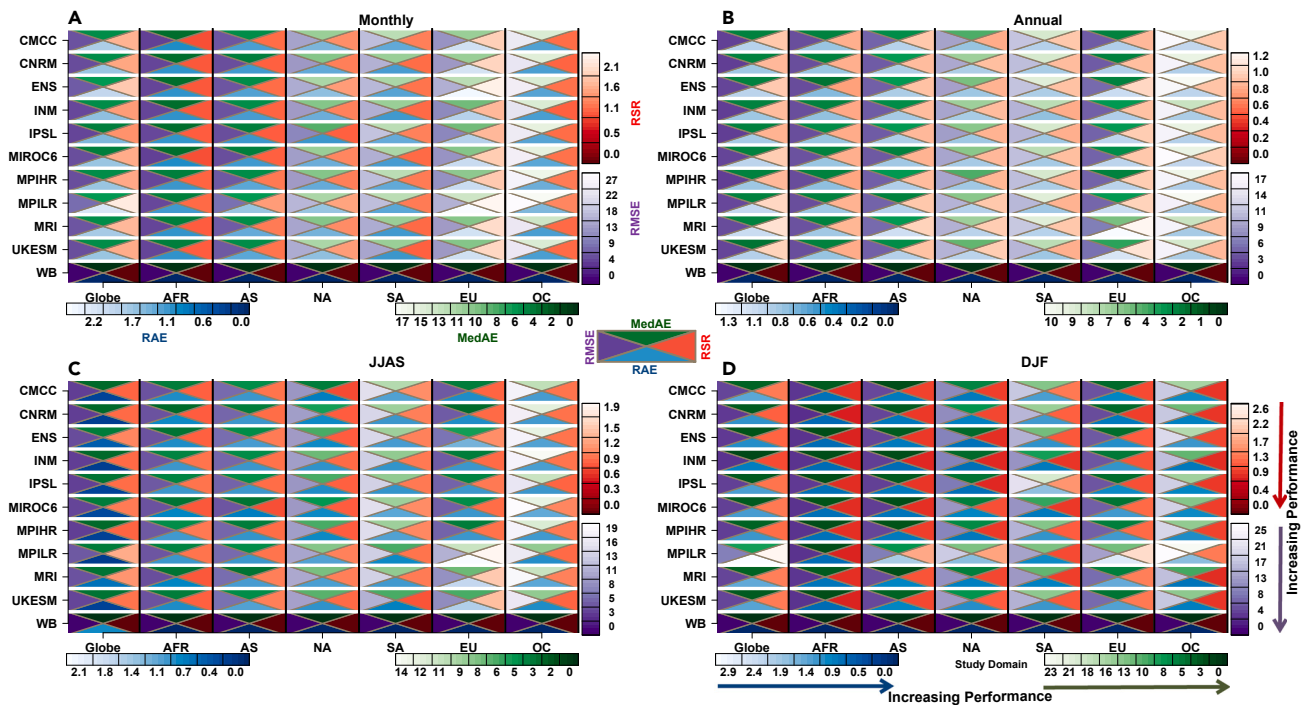
Figure 1. Performance of BC methods and global climate models for WS
The error matrix evaluates the performance of MBCN-corrected CMIP6 models in estimating derived WS across different time scales and regions:(A) monthly, (B) annual, (C) June-July-August-September (JJAS), and (D) December-January-February (DJF). Regions are denoted by AFR for Africa, AS for Asia, NA for North America, SA for South America, EU for Europe, and OC for Oceania. The graphical representation includes various triangular markers: green triangles at the top depict median absolute error (MedAE), blue triangles at the bottom represent relative absolute error (RAE), purple triangles on the left indicate root-mean-square error (RMSE), and red triangles on the right signify the RMSE-observations standard deviation ratio (RSR). For instance, the MPILR model exhibits higher RSR and RAE values (lighter colors) globally than other models on a monthly scale (A), suggesting its relatively lower accuracy in simulating derived WS monthly. WB refers to changes in WS derived from the water balance equation using reference water budget variables. In comparison with uncorrected or QDM-corrected GCMs (Figures S2 and S3), the MBCN BC technique notably minimizes biases in GCMs, maintains the interdependency among water budget variables (e.g., precipitation, evapotranspiration, and runoff), and achieves satisfactory closure in the water budget. Refer to Table S1 for the complete names of global climate models (GCMs). CNRM6, Centre National de Recherches Météorologiques CM6-1; IPSL, Institut Pierre Simon Laplace–Coupled Model version 6A–low resolution; MIROC6, Model for Interdisciplinary Research on Climate version 6; MPI-HR, Max Planck Institute Earth System Model for the High-Resolution Model Intercomparison Project (high resolution); MPI-LR, Max Planck Institute Earth System Model for the High-Resolution Model Intercomparison Project (low resolution); ENS, multi-model ensemble mean of the previous nine models.

RMSEs in Greenland can be attributed to the water budget equation's inaccurate representation of frozen WS.[48] Generally, for cold, snow-prone, and some polar regions, permafrost storage contributes to large RMSE.[48]

The identified uncertainties were effectively addressed to ensure a comprehensive closure of the water budget. Additionally, a performance evaluation of the bias-corrected GCMs using the N-dimensional probability density function transform method (MBCN; Figure 1) reveals a significant reduction in biases compared with the uncorrected GCMs (Figure S2) across various time scales, including monthly, seasonal, and annual. Notably, the MBCN-corrected GCMs demonstrate monthly performance scores ranging from 0.0 to 2.1 for the RMSE between the reference and model output and the reference standard deviation (RSR). The RMSE varies from 0.0 to 27.0 mm, the median absolute error (MedAE) ranges from 0.0 to 17.0, and the relative absolute error (RAE) varies from 0.0 to 2.5. We observe similar tendencies in the quantile delta mapping (QDM)-corrected CMIP6 models (Figure S3). Conversely, the uncorrected CMIP6 models exhibit monthly RSR ranging from 1.1 to 5.0, RMSE ranging from 7.0 to 42.0 mm, MedAE ranging from 5.0 to 36.0, and RAE ranging from 1.18 to 5.5.

Following the BC, the models with the poorest performance on a global scale are MPILR (monthly), MRI (Meteorological Research Institute Earth System Model Version 2.0) and MPILR (June-July-August-September [JJAS]), and MPILR (December-January-February [DJF]). It is worth noting that the BC methods effectively reduced uncertainties in the water budget and improved the alignment between the bias-corrected WS derived from the water budget equation (bias-corrected WS [BCWS]) and the WS data reconstructed from the GRACE mission across all temporal scales (Figures 1 and S3). This is consistent with Xiong et al.,[49] who demonstrated improved accuracy of downscaled and bias-corrected climate model simulations relative to GRACE reference data over the Yangtze River Basin.

Furthermore, there is compelling evidence of comparable statistical properties between the monthly GRACE data and the MBCN-BCWS (Figure 2) that validate the reduction in uncertainty at the basin scale. The breadth of each density curve corresponds to the estimated frequency of data points within an area.[50]
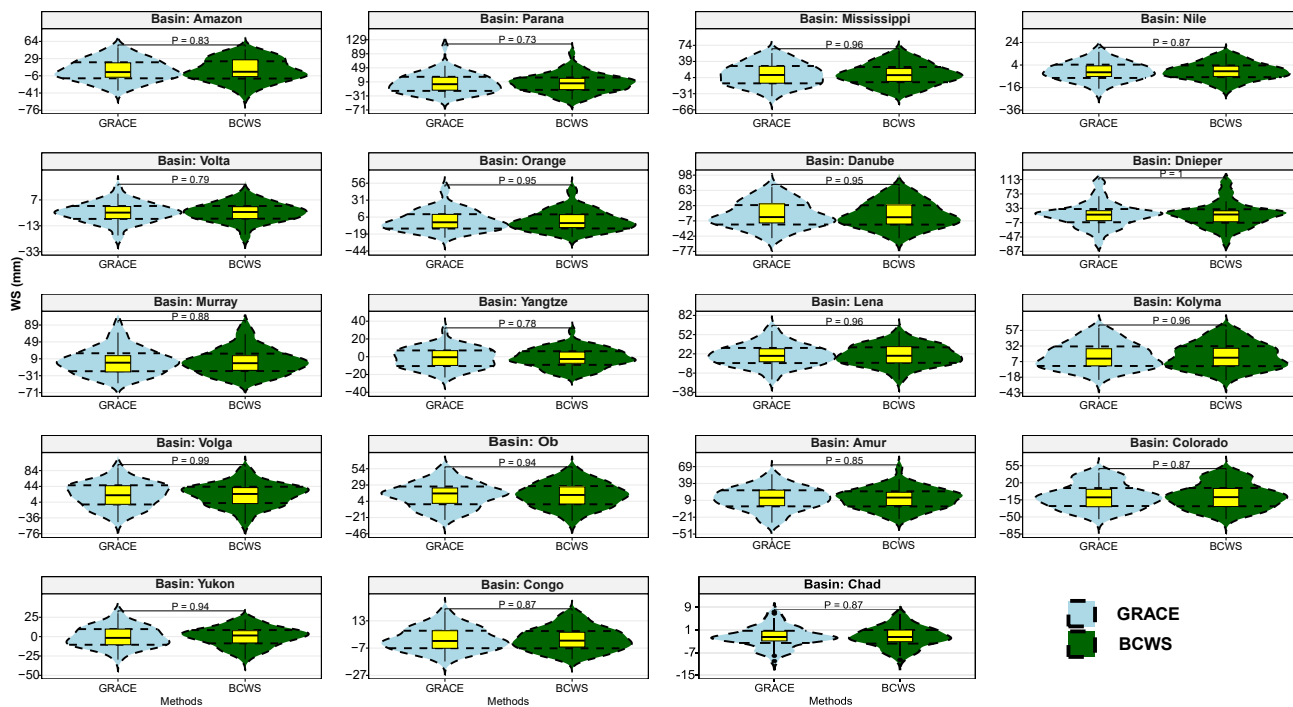
Figure 2. Basin-scale performance of monthly GRACE and the MBCN-bias-corrected WS
The width of each density curve represents the estimated frequency of water storage (WS) change data points within a specific area. We can gauge similarities or differences in the data series by comparing the peaks, troughs, and tails of these density curves. The blue density curves represent WS from the Gravity Recovery and Climate Experiment (GRACE), while the green density curves depict MBCN-bias-corrected WS (BCWS) obtained from the water budget equation. Significant changes in the mean, calculated using a t test, are shown on the horizontal line between the two plots for each basin. The p value represents the threshold at which the null hypothesis (no difference between the mean values of monthly GRACE and MBCN bias-corrected WS) is rejected. The figure presents strong evidence of similar statistical properties between the data sources, confirming reduced uncertainty at the basin scale.

Comparing the peaks, troughs, and tails of these density curves allows us to assess similarities or discrepancies in the data series.[50] A broad density curve suggests a high frequency of values within a particular range, while a narrow density curve indicates a lower occurrence of values in that range.[50] We observe notable similarities in the properties of the density curves and no significant alterations in the mean values across all basins (p > 0.05). This lack of significant mean changes between the GRACE data and the BCWS underscores the effectiveness of the BC method in accurately addressing water budget errors arising from utilizing water budget variables from diverse sources. In general, multivariate BC can effectively enhance the consistency, precision, and dependability of climate model simulations[4,33,35,42] while reducing the uncertainties arising from water budget closure. Furthermore, the Student's t test statistic at a 95% confidence level is used to evaluate GRACE and MBCN-BCWS data, and the analysis indicates no statistically significant difference in the annual WS for most models across various regions (Figure S4). Consequently, the CMIP6 multimodel ensemble mean (Figure S4C) and INM (Institute for Numerical Mathematics CM5) (Figure S4D) demonstrate the overall best performances. Even though single-model, initial-condition, large ensembles quantify uncertainty from the model's internal variability,[51] that single model may be an inadequate approximation of reality. In contrast, multimodel ensembles generate climate simulations with identical forcing across multiple models to quantify epistemic uncertainties. Therefore, conducting

thorough model evaluation and implementing BC is crucial when utilizing either of the two ensemble approaches for impact assessment.[4,37,42,47,51] Therefore, we use the CMIP6 multimodel ensemble mean (ENS) (Multi-model ensemble mean of the previous nine models) in the subsequent sections after establishing the overall robustness in the previous analyses.

Joint dependency structure and partial correlation
Ensuring that the ENS and BC methods can accurately capture and preserve the dependency structures among water budget variables, such as precipitation, actual evapotranspiration, and runoff, is crucial. However, the QDM-corrected ENS fails to preserve the dependency between WS and actual evapotranspiration for all continents (Figure S5A). In contrast, the MBCN-corrected ENS maintains this dependency, with values close to zero observed for every continent (Figure S5B). On the other hand, the uncorrected ENS cannot retain the dependency structure between WS and other variables (Figure S5C). A higher RMSE generally indicates a more remarkable inability of the model to preserve the joint dependency structure among the variables.

We also show that the bias-corrected ENS effectively preserves the partial correlation between WS and precipitation (Figure S6). However, the uncorrected ENS fails to replicate this relationship, particularly in Asia and North America, potentially leading to mischaracterizing basins such as the Volga, Ob, Lena, and Mississippi (Figure S6C). Generally, the reference dataset and the

MBCN bias-corrected ENS have a positive partial correlation between WS and precipitation across all basins (Figures S6B and S6D). This positive correlation between WS and precipitation, along with the predominantly negative correlation with actual evapotranspiration, can be influenced by changes in temperature. As the temperature rises, more moisture is introduced into the atmosphere through evapotranspiration, propelling a precipitation event via moisture convergence at lower altitudes and resulting in heavier precipitation.[23,52,53] Therefore, more water is available because of the high intensity and flow of the recent precipitation event;[23] hence, the positive correlation between WS and precipitation and the majorly negative correlation with evapotranspiration[54] in the reference and MBCN bias-corrected ENS.

Moreover, both the QDM-corrected and uncorrected ENS demonstrate inadequate performance in evaluating the correlation between WS and runoff (Figures S6A and S6C). This inadequacy stems from inherent biases within the uncorrected CMIP6 models, compounded by the limitations of QDM in rectifying biases sequentially across all variables.[33] Hence, the association among the variables is missing during QDM corrections.[33,42,43,55] Conversely, MBCN preserves the multivariate dependence structure reasonably well.[33,43] Generally, small precipitation amounts and high evaporative demand can result in low WS. Likewise, high precipitation and low evaporative demand can cause low evapotranspiration and high WS, aiding rapid soil recharge. Also, a high volumetric water content threshold is required for runoff activation in deeper tropical soil layers.[56] Increased precipitation over tropical soils with high drainable porosities keeps the volumetric water content at saturation. When the saturation threshold at lower soil depths is exceeded, the extra water flows to the upper levels, satisfying the field capacity, and runoff begins.[56] On the other hand, drainable porosity declines with depth in temperate soils due to increases in bulk density,[57] triggering a quick rise in the water table and accelerating shallow lateral subsurface flow;[57] hence, the positive partial correlation between runoff and WS.

Historical WS trends and future projections

The analysis of the WS annual trend (Figure S7) reveals notable differences between the uncorrected ENS and the reference dataset. In the historical period, the uncorrected ENS overestimates the trends in most basins. For instance, the reference dataset indicates predominantly negative trends ranging between −25 and 0 mm/decade in basins such as the Amazon, Chad, and Colorado (Figure S7A). However, the uncorrected ENS classifies these trends as ranging between −5 and 15 mm/decade (Figure S7B). In contrast, the MBCN-corrected ENS satisfactorily replicates these observed trends (Figure S7C). These trends are consistent with past studies, including over China,[32] where similar negative trends have been reported. The significance of the observed trends varies across basins, with the corrected ENS consistently detecting more accurate and significant trends than the uncorrected ENS. Therefore, the MBCN-corrected ENS proves reliable for effectively illustrating future trends in WS. Under the shared socioeconomic path (SSP) 245 scenario, significant negative trends are observed in some parts of the Amazon, Paraná, Nile, and Volta basins (Figure S7D). These negative trends are further intensified under the SSP 370 and 585 climate change scenarios. The trends for different seasonal classifications (JJAS and DJF) are also evaluated and are consistent

with the reference data, demonstrating the accuracy of MBCN-corrected ENS.

Furthermore, analyzing multiple-period trends for selected basin averages (Figure 3) reveals magnitude and trend significance variations during the JJAS season. Specifically, the Yangtze River basin exhibits mixed trends in the historical period, as seen in the JJAS single-period trend (Figure S8). However, the negative trends observed in the multiple-period analysis are statistically significant (Figure 3A I). For instance, the Yangtze River basin manifests a positive but non-significant trend of 7 mm/decade from 1959 to the later 30-year period (along the y axis). In contrast, the 56-year period indicates a non-significant −2 mm/decade trend. Additionally, future projections from 2057 to 2070, under the SSP 245 scenario, exhibit predominantly positive trends (Figure 3B I). However, under SSP 585, although significant trends are absent, we observed a greater number of positive trends than the SSP 245 scenario (Figure 3D I).

On the other hand, the Amazon basin exhibits significant negative trends for all years under all future SSPs (Figures 3B–3D, ii). Notably, there are some positive trends during drought episodes (in the 1970s) in the Lake Chad basin (Figure 3A, iii). This can be attributed to the rising groundwater table despite prolonged droughts, a phenomenon popularly called the Sahelian paradox.[58] This also enhances vegetation recovery during that period.[59] In addition, the warming of the northern Atlantic Ocean and the Mediterranean Sea positively impacts the Lake Chad basin by boosting the meridional convergence of external moisture at low levels.[27,60] As a result, the region experiences increased precipitation and a partial rebound of rainfall after drought episodes.[23] Similarly, positive WS trends can be attributed to increased soil moisture content due to increasing rainfall intensity from the intensification of the low-level jet in the area.[61] However, the local moisture recycling rate, regulated by planetary flow patterns coupled with the El Niño-Southern Oscillation, significantly impacts annual precipitation fluctuations in the basin.[23,62] Figure S9 illustrates the single-period trend for the DJF season, noting consistent negative trends in the Amazon, Paraná, and Nile basins for the historical and all future scenarios.

WS and LULC classification

Following the initialization, competition, collaboration, self-organization, and clustering adaptation mechanisms of the WS self-organizing maps (SOMs),[31] we classified the WS into 11 units (Figure 4). In the historical JJAS, basins such as the Amur and Volta witness an extreme WS surplus. Moreover, LULC type is also an important factor in WS representation. For example, basins with a high proportion of forest cover (Amazon, Congo, and Volga; Figure 5) are generally linked with a WS deficit in the JJAS period. This can be attributed to less precipitation reaching the ground due to tree canopies and increased evapotranspiration due to active tree transpiration and higher leaf area.[27,63] Hence, the recharge appears to be slower. Also, lower temperatures, limited water availability from frozen soil or reduced precipitation, snowfall interception, and decreased leaf area index can prevent high evapotranspiration rates,[64] thereby maintaining WS in DJF. It is important to note that the WS deficit in forested basins varies depending on forest type. For example, broadleaf forests facilitate more WS deficit than other vegetation types (cf. Figures 4A and 5). Additionally, the type of vegetation, its height,
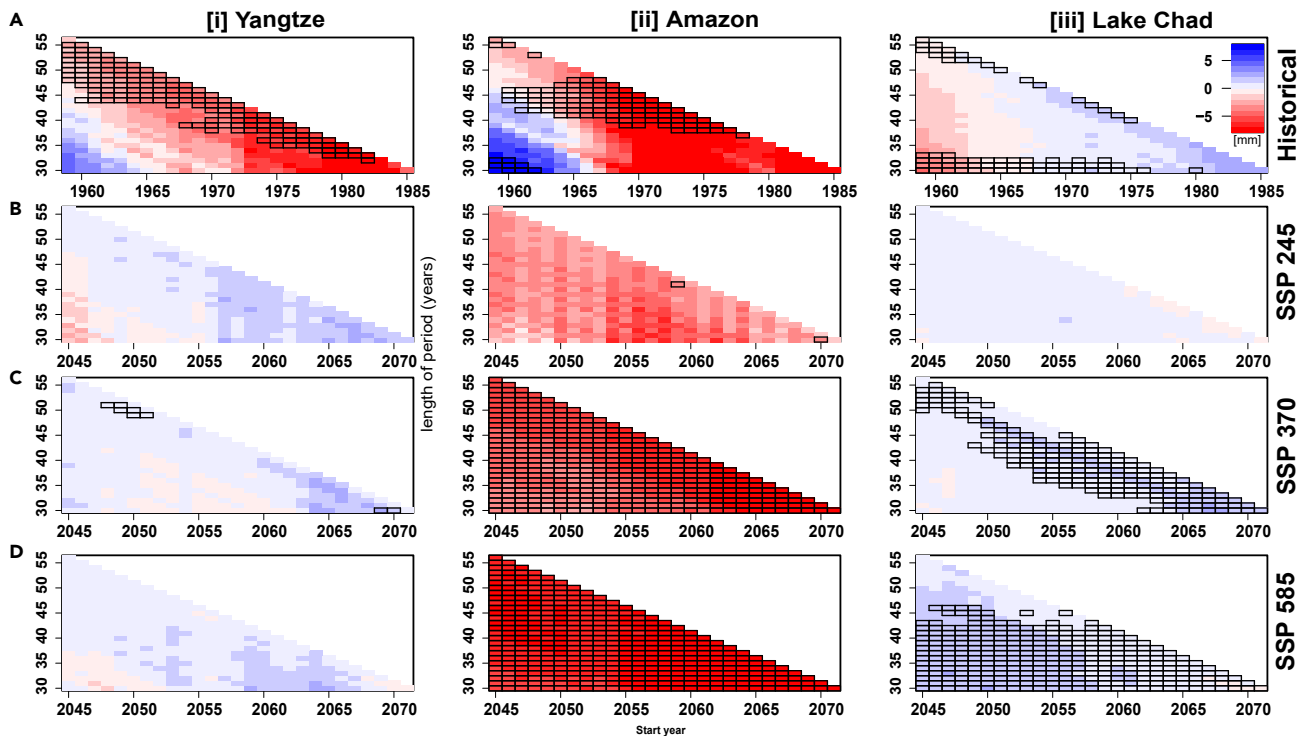
Figure 3. Changes in WS trends (mm/decade) during historical and future projections for the JJAS season

Shown are 30-year multiple-period WS trends (mm/decade) in the (i) Yangtze, (ii) Amazon, and (iii) Chad basins for the (A) historical period, (B) future period under SSP 245, (C) future period under SSP 370, and (D) future period under SSP 585. The y axis shows the duration of each period and its corresponding starting points on the x axis. The time series are based on the spatial mean aggregation of the basins. The results are visually presented on a grid, with the x and y axes representing the starting point and length of each period, respectively. The color scale indicates the strength of observed trends, with black outlines highlighting periods demonstrating significant trends at the 99% confidence level. This displays trends across various timescales, considering start and endpoint variations. The uppermost left corner represents the longest duration of the time series, while the lowermost right corner indicates the most recent period. As exemplified in this figure, it is evident that the robustness and statistical significance of estimated trends are contingent on the specific time frame under examination. Therefore, the multiple-period trend analysis is a more robust alternative to single-period trend fitting.[50] For instance, in the Yangtze basin, a 30-year period starting in 1959 shows a positive WS trend of about 7 mm/decade. However, with the entire 56-year time series, the trend becomes slightly negative. This highlights how series length impacts trend calculations and illustrates regional variations in WS trends. Specifically, we observed reductions in WS for the Yangtze and Amazon basins, while a marginal decrease is noted for the Lake Chad basin. Climate projections indicate severe and statistically significant decreases in WS for the Amazon basin in the future, while slight increases are projected for the Yangtze and Lake Chad basins.

and its density are key factors that significantly influence the accumulation and interception of snow and precipitation.[65]

On the other hand, basins with a high proportion of combined grassland, shrubland, and barren land are linked with JJAS WS surplus (e.g., Volta and Ob). However, shrublands in the polar basins (e.g., Yukon, Kolyma) aid more WS deficit in the JJAS season. In general, leaf area increases precipitation and snow interception, but tall shrubs promote snow trapping.[65] Furthermore, the WS classification is reversed for many basins during the DJF season (Figures 4B and 5). This suggests that the WS modifications are not based solely on LULC type but also on seasonal differences in climate dynamics.

In the future JJAS under SSP 245, most basins in the Southern Hemisphere will experience more intense WS deficits. At the same time, North Africa will reverse from a slight surplus (Figure 4A) to a severe WS deficit (Figure 4C). It is worth noting that, under SSP 370 JJAS, several basins, like the Kolyma, that previously experienced WS deficits during the historical period show a shift in signals during the future period. Therefore, further investigation is needed to understand the underlying mechanism behind these dy-

namic patterns. On the other hand, most tropical basins show a northward shift of the WS surplus under SSP 585. Notably, most basins in the Southern Hemisphere get drier, while basins just above the equator get wetter, confirming the "dry gets drier and wet gets wetter" paradigm.[41] For future DJF seasons, the WS surplus recovers in the tropics, shifting farther north under SSP 585, while the extreme WS deficit is more pronounced under SSP 245. Most Southern Hemisphere basins witness wetter conditions under SSP 370 compared with SSP 245 and 585. Because CMIP6 model projections incorporate future LULC dynamics, changes in future LULC could be essential in WS future classifications.

WS and climate dynamics

Given the established WS feedback from LULC, a critical emphasis lies in comprehending the impact of climate dynamics on WS. Figure 6 shows the seasonal, long-term average state of wind fields, WS, and geopotential height in the lower and mid-troposphere from 1959 to 2014. Investigating the Northern-Hemispheric tropical African expanse reveals a strong lower tropospheric southwesterly monsoon wind from the Atlantic
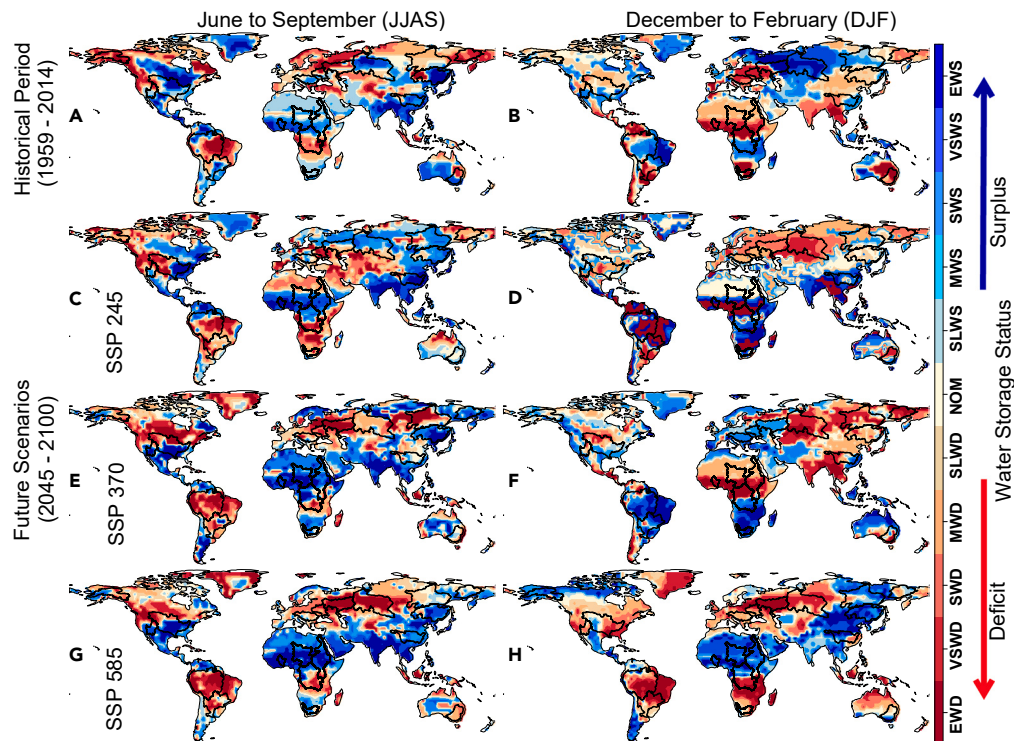
Figure 4. WS classification

Seasonal WS classifications are based on the self-organizing maps and GMM for (A) the JJAS historical period, (B) the DJF historical period, (C) JJAS future projection under SSP 245, (D) DJF future projection under SSP 245, (E) JJAS future projection under SSP 370, (F) DJF future projection under SSP 370, (G) JJAS future projection under SSP 585, and (H) DJF future projection under SSP585. The black polygons represent the river basins. EWD, extreme WS deficit; VSWD, very strong WS deficit; SWD, strong WS deficit; MWD, moderate WS deficit; SLWD, slight WS deficit; NOM, normal condition; SLWS, slight WS surplus; MWS, moderate WS surplus; SWS, strong WS surplus; VSWS, very strong WS surplus; EWS, extreme WS surplus. In the future JJAS season under SSP 245, most basins in the Southern Hemisphere are projected to experience intensified WS deficits compared with the historical period. Tropical basins are expected to witness a northward shift in WS surplus under SSP 585, indicating drier conditions in the Southern Hemisphere and increased moisture slightly above the equator. During future DJF seasons, tropical regions exhibit a further northward shift in WS surplus under SSP 585, while SSP 245 portrays extreme WS deficits. Most Southern Hemisphere basins showcase wetter conditions under SSP 370 compared with SSP 245 and 585. These findings highlight significant shifts in water availability across basins, signaling an impending increase in aridity for many Southern Hemisphere areas and a trend toward wetter conditions near the equator during JJAS. This emphasizes the critical need for targeted and region-specific approaches in managing water resources amid changing climate dynamics. See Figure 5 for basin names.

Ocean during JJAS (Figure 6A), carrying moisture inland. This is accompanied by a monsoon trough centered on the Sahel, a weak ridge across the Mediterranean Sea, and southward moisture transport (Figure 7A). This favors the wetting of this region, thereby stimulating WS surplus in JJAS (Figure 4A).

Furthermore, the southwestern monsoon pushes moisture up to around 18°N[66] (Figure 6A), while southward moisture transport from the Mediterranean Sea dominates the larger expanse of the Sahel (Figure 7A). In the mid-troposphere, there is a Saharan high to the west, favoring the intensification of the African easterly jet (AEJ) (Figure 6C).[67] This increases the magnitude of the southward moisture transport westward from the Mediterranean Sea by around 80 kg/m²/s (Figure 7A). On the other hand, moisture transport from the Atlantic Ocean, orchestrated by the southwesterlies, is limited to the lower troposphere[68] (Figure 6A). As a result, the lower tropospheric southwestern monsoon governs WS dynamics in the southern Volta, southern Chad, and southern Nile basins.

In contrast, the weak ridge in the lower troposphere, AEJ,[69] and the Saharan high in the middle troposphere regulate moisture intake in the northern Chad and northern Nile basins. The Nile basin has substantial moisture influx from the northern, eastern, and southern boundaries, while the western boundary is the export channel (Figure 7A). The intensity of the northward moisture fluxes at the southern boundary is greater than that of the inward moisture fluxes at the northern boundary or the outward moisture fluxes at the western boundary.[66] This suggests that the leading cause of the high water vapor content during JJAS is the northward moisture flux linked to the Indian monsoon (Figures 6A and 7A). This demonstrates that the Indian Ocean is one of the most crucial sources of moisture for the rising moisture content in this basin. The cutoff highs and the tropical cyclones around Madagascar (Figure 6A) and low-level jet[70] in the lower troposphere redirect substantial moisture from the Indian Ocean away from Madagascar and East Africa toward the Nile basin (Figure 7A). Nevertheless, this phenomenon triggers the displacement and intensification of the low-level jets in DJF, notably toward the southern regions of Madagascar (Figure 6B). This displacement results in abundant moisture inflow, closely associated with atmospheric rivers from the Indian Ocean into the southern Congo basin in DJF (Figure 7B). While
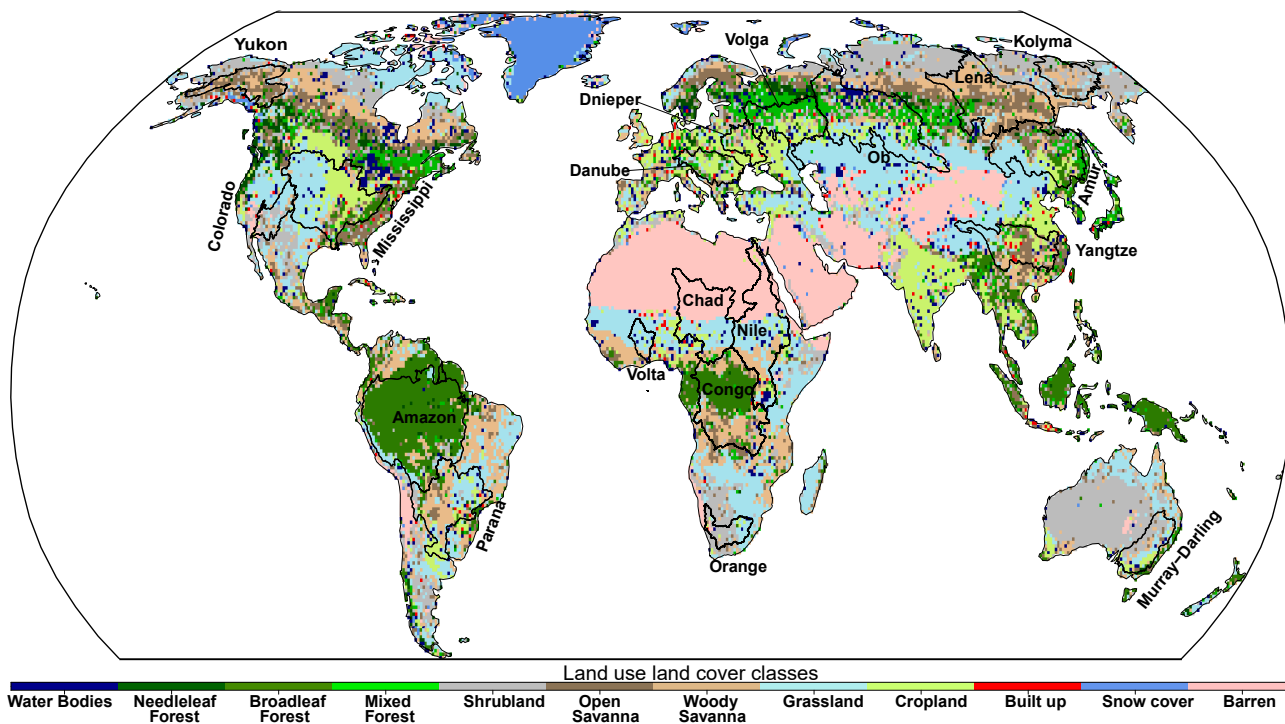
Figure 5. Land use and land cover classes
We reclassified the International Geosphere-Biosphere Program (IGBP) type 1 scheme global land use and land cover (LULC) dataset identifying 11 natural vegetation classes, three developed and mosaicked land classes, and three non-vegetated land classes into 12 distinct categories based on their similarity intervals to enhance interpretability. The black polygons represent river basins. LULC type is a crucial factor influencing WS changes. Basins with more forest cover (e.g., Amazon and Congo) consistently display a WS deficit during the historical JJAS period (Figure 4). The WS deficit within forested basins varies based on the specific forest type. Broadleaf forests exhibit higher WS deficits than other vegetation types (refer to Figure 4A for a detailed comparison). Basins dominated by grassland, shrubland, and barren land (e.g., Volta and Ob) consistently show a WS surplus during JJAS (Figure 4). These findings highlight the intricate relationship between LULC characteristics and WS patterns, highlighting the need for region-specific WS management strategies.

more moisture is available from atmospheric rivers, this does not always translate to surplus WS due to different LULC classes, atmospheric river characteristics, and landfall zones.[71] Generally, the increased greenhouse warming from abundant moisture increases temperature.[72] As a feedback, waterbodies lose more water due to higher evaporation, thereby increasing atmospheric moisture content.

The Amazon basin primarily receives inflow from its northeastern boundary during the JJAS period. In contrast, the other boundaries predominantly experience strong outflows (Figure 7A). Interestingly, the substantial outflows from the Amazon's southern boundary, which result in a WS deficit in the Amazon basin, play a pivotal role as inflow for the Paraná basin, thereby leading to a WS surplus in Paraná (Figures 4 and 6). This robust outflow from the Amazon subsequently continues toward the southern boundary of the Paraná basin. The South America coastal jet[73] (Figure 6C) dominates the moisture inflow and outflow (Figure 7A), while the low tropospheric anti-cyclonic vortex (Figure 6A) regulates the direction of flow over these basins. During DJF, the easterly crosses northern Australia, causing rapid moisture inflow from the western Pacific Ocean (Figure 7B). However, the low tropospheric low-pressure center (Figure 6B) and mid-tropospheric high-pressure center (Figure 6D) associated with this region during this period converge the moisture in

northern Australia, paving the way for a robust westward outflow toward northwestern Australia (Figures 6B and 7B).

The dominant northward moisture inflow into the Yangtze and Amur basins in JJAS (Figure 7A) is from the South China Sea,[74] aided by the low-level ridge and strong monsoon wind (Figure 6A). However, the Bay of Bengal, a low-level trough, and a mid-level jet (Figures 6B and 6D) are prominent in the northward moisture influx into the Yangtze and the moisture cutoff to the Amur in DJF (Figure 7B). Additionally, the Asian westerly jet (Figure 6D) and low-level high-pressure center in central Asia (Figure 6B) strengthen the transport of the northward-flowing moisture from the Arabian, Mediterranean, and Red Seas toward the Volga and Ob during DJF (Figure 7B), thereby enhancing the WS surplus in these months (Figure 4B).

We note higher moisture transport values over subtropical continents in both hemispheres.[71] However, we observe a maximum landfalling atmospheric river on the western coast of the Atlantic, where high sea surface temperatures support a faster evaporation rate, supplying moisture to the atmosphere and promoting its subsequent transit to other places.[71] This area is a crucial moisture pool for North Atlantic Ocean atmospheric rivers landfalling on the western European coast, northeastern American coast, Iceland, and Greenland.[71] It is important to note that large atmospheric rivers are not synonymous with high precipitation extremes, as many
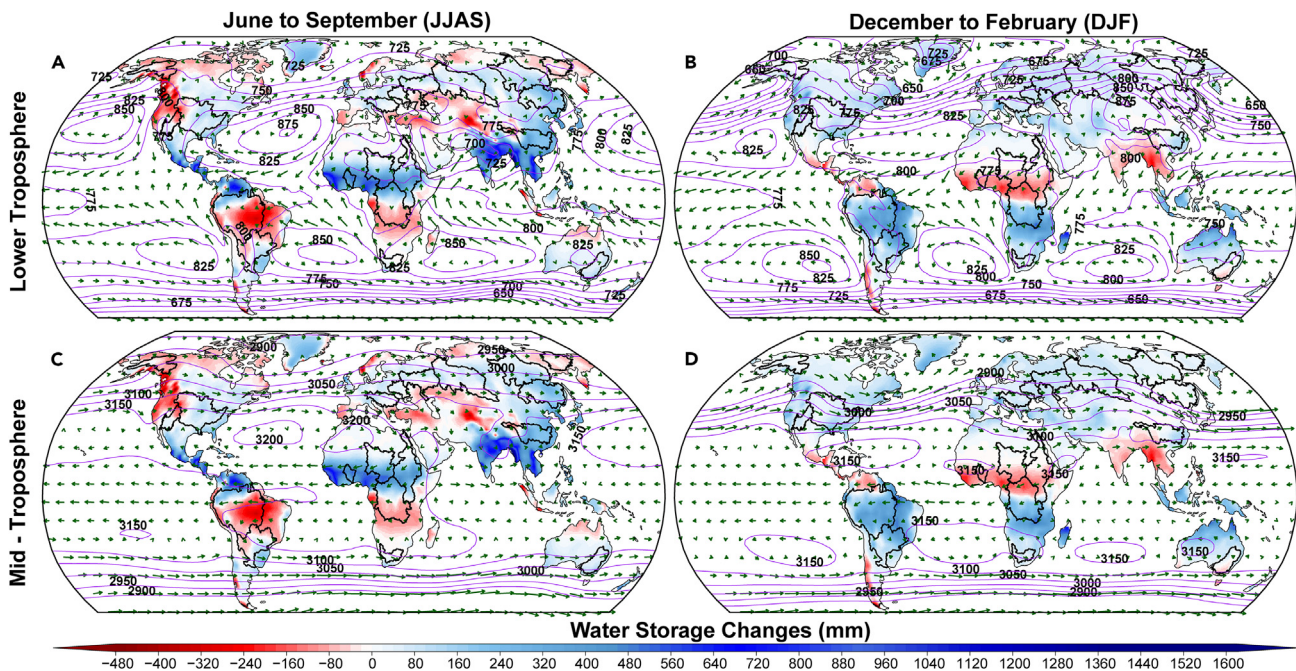
Figure 6. WS and climate dynamics

Shown are the long-term average states from 1959 to 2014 of WS (mm) (background), wind fields (m/s) (green vectors), and geopotential height (m) (purple contours and black labels) in the lower troposphere (925 hPa) for (A) JJAS and (B) DJF and in the mid-troposphere (700 hPa) for (C) JJAS and (D) DJF. The black polygons represent river basins. See Figure 5 for basin names. Changes in WS dynamics are significantly shaped by monsoonal winds, atmospheric pressure, and high-altitude winds (jets). This interplay is crucial in various basins where distinct atmospheric phenomena notably influence WS dynamics. For instance, WS dynamics are steered primarily by the effects of the lower tropospheric southwestern monsoon in basins like the southern Volta, southern Chad, and southern Nile. In the northern Chad and northern Nile basins, factors like the weak ridge in the lower troposphere, the AEJ, and the Saharan high in the middle troposphere regulate moisture intake. These unique atmospheric conditions underscore the distinct and intricate influences affecting WS dynamics across different regions. This highlights the importance of comprehending localized atmospheric mechanisms governing WS in specific basins.

non–atmospheric river events have been associated with more extreme precipitation occurrence.[75] More importantly, enhanced moisture drives the fast warming of the near-surface temperature,[61] thus accelerating evaporation, which could potentially lead to more WS surplus. Moreover, this also depends on other dynamic factors, like the origin of the transport and the area of landfall.

Conclusion

We investigate global WS using bias-corrected CMIP6 GCMs. Our findings demonstrate that the MBCN BC technique effectively reduces biases in GCMs, preserves the dependency structure of WS variables (e.g., precipitation, evapotranspiration, and runoff), and achieves satisfactory water budget closure, offering a versatile methodology for the climate and hydrology research community. However, it is worth noting that the complexity of the MBCN method makes it time consuming and computationally demanding.[33,35,42,43] Nevertheless, it is essential to conduct robust evaluations to ensure that the various WS properties are preserved while solving the water budget problem. This is crucial for maintaining accuracy in WS representativeness. For instance, QDM-corrected WS successfully maintains the quantity of WS but cannot preserve its dependency structure with other water budget variables. In general, multi-variate BC can effectively enhance the consistency, precision, and dependability of climate model simulations[4,33,35,42] while reducing the uncertainties arising from water budget closure.

Additionally, we establish that WS dynamics are influenced by geographical area, LULC type, and climate dynamics that affect moisture movement in and out of basins. It is important to note that additional moisture intake into basins does not always lead to surplus WS due to various local-scale impacts, different LULC classes, atmospheric river characteristics, and landfall zones. Furthermore, we observe varied trends in WS across different basins, with the corrected model revealing more significant and accurate trends than the uncorrected CMIP6 multimodel ensemble mean. Under SSP 245, the future JJAS season exhibits more severe deficits in most basins in the Southern Hemisphere, while basins in North Africa experience a notable shift from a slight WS surplus to a severe WS deficit compared with the historical period. In contrast, under SSP 585, there is a northward shift in WS surplus in most tropical basins. Notably, basins in the Southern Hemisphere experience drier conditions under SSP 245, while African basins just above the equator become wetter across all climate scenarios compared with the historical period. For the future DJF season, the WS surplus in the tropics recovers and shifts farther north under SSP 585, while a severe WS deficit remains evident under SSP 245. Under SSP 370, most basins in the Southern Hemisphere exhibit wetter conditions compared with the historical period.

These findings offer insight into how ecological and human systems dependent on these WS dynamics could be affected.
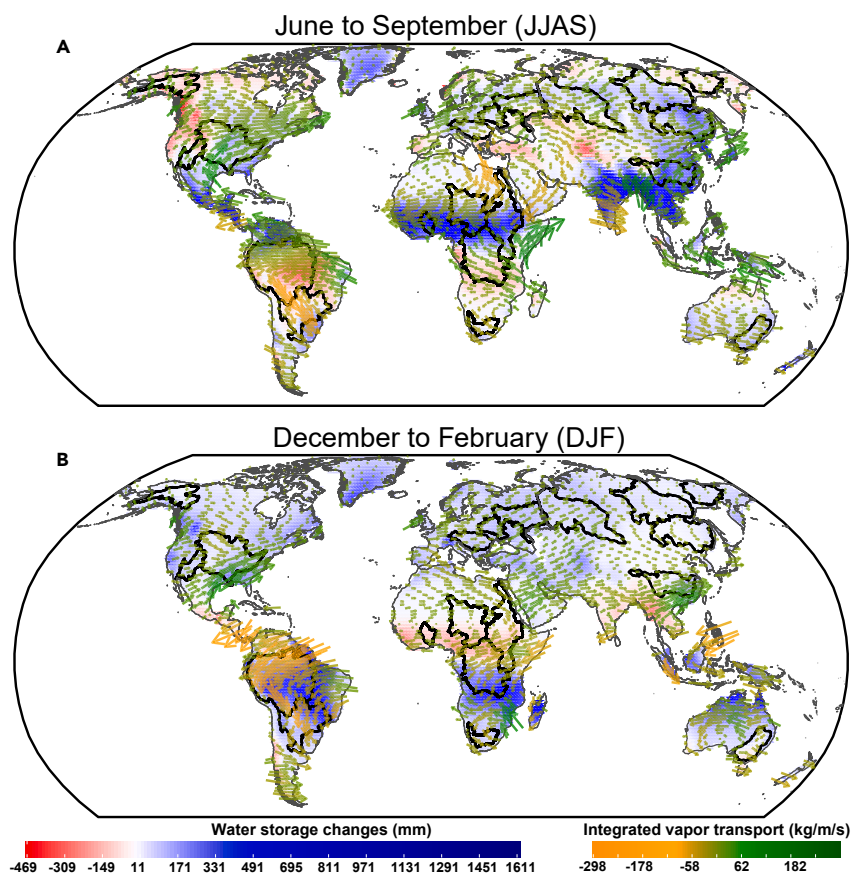
June to September (JJAS)

A

December to February (DJF)

B

Water storage changes (mm)

-469 -309 -149 11 171 331 491 695 811 971 1131 1291 1451 1611

Integrated vapor transport (kg/m/s)

-298 -178 -58 62 182

Figure 7. WS and vapor transport

Shown are long-term average states from 1959 to 2014 of WS changes (mm) (background) and integrated vapor transport (IVT; kg/m/s) in vectors during the historical (A) JJAS and (B) DJF seasons. Negative IVT means southward moisture transport, while positive IVT means northward moisture transport. The black polygons represent river basins, and the background is WS changes. See Figure 5 for basin names. Comprehending the dynamics of moisture transport is integral for understanding the movement of moisture into and out of basins. For example, during JJAS, the increased moisture content in the Nile basin is supported by the northward moisture transport from the Indian Ocean. This underscores the importance of the Indian Ocean as a primary moisture source for improving moisture conditions in the Nile basin. While atmospheric rivers contribute to increased moisture availability, this does not uniformly lead to excess WS due to variations in land use and land cover, differing features of atmospheric rivers, and the locations where they land. This complexity is evident in the southern boundary of the Amazon, where substantial outflows result in a WS deficit. However, these outflows are a significant inflow for the Paraná basin, contributing to the Paraná basin WS surplus during JJAS. These observations highlight the intricate relationship between moisture transport, land characteristics, and resulting WS dynamics in basins. It emphasizes the need for a thorough understanding of these complex interactions to effectively manage water resources in different regions.

Conserved water is crucial in lake and wetland systems, agriculture, shallow groundwater recharge, and irrigation. WS dynamics greatly influence associated ecological and social structures, including wetland maintenance, groundwater replenishment, lake health, irrigation scheduling, and improved water management in agriculture. The projected deficits or surpluses in WS due to climate change will impact water supply and may enhance or imperil the efficiency of hydrological and agricultural systems. Policymakers can consider the effects of WS dynamics when formulating climate change adaptation or mitigation strategies for different subsystems. Furthermore, sustainable land management approaches that promote ecosystem services and safeguard biodiversity should also be supported.

EXPERIMENTAL PROCEDURES

Resource availability

Lead contact

Requests for further information and resources should be directed to and will be fulfilled by the lead contact, Wen Zhou (wen_zhou@fudan.edu.cn).

Materials availability

This study did not create any new or distinctive materials.

Data and code availability

The CMIP6 data and codes are publicly available through the Earth System Grid Federation at http://esgf.llnl.gov/.

The CRU reference data are publicly available at https://crudata.uea.ac.uk/cru/data/hrg/#info.

The reconstructed GRACE data are publicly available at https://doi.org/10.6084/m9.figshare.7670849.

The Global Runoff Ensemble (GRUN) reference data are publicly available via https://doi.org/10.6084/m9.figshare.9228176.

The JRA55 reference data are publicly available at https://rda.ucar.edu/datasets/ds628.1/.

The Moderate Resolution Imaging Spectroradiometer (MODIS) dataset is publicly available at https://lpdaac.usgs.gov/tools/usgs-earthexplorer/.

The code used in this manuscript is deposited and freely available at https://github.com/cyndyfem/One-Earth-Paper.git and publicly available as of the publication date.

The original and unprocessed climate data used for this study are available in Adeyeri.[76]

Upon request, the lead contact will provide any extra data necessary to reanalyze the data described in this study.

Variables

Our analysis centers on nine CMIP6 models and their ensemble means for the SSP 245, 370, and 585 scenarios[77] for the historical (1959–2014) and future (2045–2100) periods (Table S1). The monthly reference dataset for precipitation and temperature is based on the Climate Research Unit (CRU) series.[78] The reference runoff is based on the GRUN[79] at 0.5° resolution. The Japanese 55-year Reanalysis (JRA55)[80] monthly fields of specific humidity (q), zonal and meridional winds (u, v), geopotential height, and actual evapotranspiration at a 1° × 1° grid resolution are used to calculate the moisture transport and water budget. The reconstructed changes in terrestrial WS[68] from the GRACE are used to evaluate WS from the water budget equation and bias correct the climate models. Subsequently, the monthly fields are aggregated to seasonal means. All datasets are regridded to a standard 1° ×1 ° grid to prevent erroneous scale gap effects.[34,81] All conservative variables (precipitation, runoff, specific humidity, geopotential height, and actual evapotranspiration) are regridded using the

conservative remapping technique, while the bilinear remapping technique[34,82] is used for all non-conservative variables (WS, zonal and meridional winds). The LULC data are derived from MODIS Land Cover Type (MCD12Q1) v.6.[31]

WS change

The water budget equation is initiated with three meteorological variables: precipitation, actual evapotranspiration, and runoff. This is given as

$$\frac{\delta S}{\delta t} = J - ET - Q \qquad \text{(Equation 1)}$$

where S is the total WS change over time, J is the precipitation, ET is the actual evapotranspiration, and Q is the runoff.

Due to the uncertainties related to water budget closure, especially from using different data sources, the WS generated from the climate models during the historical period is bias corrected and evaluated against the reconstructed changes in WS[83] of the GRACE mission (GRACE-REC). The GRACE missions have delivered unparalleled global estimates of monthly WS anomalies. However, due to their relatively short temporal span (~20 years), GRACE observational outputs are insufficient for evaluating the long-term trends of WS. As a result, we use the reconstructed GRACE products,[83,84] which employ statistical models in training GRACE observations to backcast previous climate-driven changes in WS using daily and monthly meteorological information. In contrast to conventional hydrological models that individually represent water reservoirs such as snow and soil moisture, typically yielding a single model run, GRACE-REC directly reconstructs total WS changes and incorporates numerous ensemble members, thereby enabling a comprehensive assessment of predictive uncertainty.[50] To assess the accuracy of these data-driven WS estimates, several studies[19,41,83,84] have independently evaluated GRACE-REC and ascertained its accuracy and robustness. GRACE-REC is provided at a spatial resolution of 0.5° from 1901 to the present.

BC

A quantile-dependent correction function between the model simulation or water budget WS quantiles and the observations quantiles is used in the univariate quantile mapping (QM) BC technique. With this function, the simulated data are converted into bias-corrected data. The underlying presumption is that models can accurately predict the variable's quantiles, or ordered categories, for both the past and future periods.[33,85–87] To preserve the relative or absolute quantile changes, QDM multiplies the modeled values by the observed values at the exact quantiles, subsequently estimating the relative or absolute quantile changes between the calibration and future periods. Consequently, multiplying these relative changes by the bias-corrected values generates the bias-corrected future projections.[33,42,43]

While preserving the anticipated changes in the simulated quantiles, multivariate BC employs the QM technique to adjust the marginal distributions of the climate model simulations. The multivariate rescaling approach is applied to modify the joint multivariate dependence structure between different dependent variables during multivariate BC.[55] The multivariate BC method using the N-dimensional probability density function transform (MBCN) expands the N-dimensional probability density function transform algorithm with QDM.[33,43] Both QDM and MBCN are used in this study.

The QDM transfer function is given as follows.[43]

The relative change in quantiles between the calibration and projected periods (t) for conservative variables is given as

$$\Delta(t_c) = \frac{F_{m,p}^{[t-1]}[\varepsilon(t)]}{F_{m,c}^{-1}[\varepsilon(t)]} \qquad \text{(Equation 2)}$$

The relative change in quantiles between the calibration and projected periods (t) for non-conservative variables is given as

$$\Delta(t_{nc}) = F_{m,p}^{[t-1]}[\varepsilon(t)] - F_{m,c}^{-1}[\varepsilon(t)] \qquad \text{(Equation 3)}$$

The non-exceedance probability (ε) associated with variable x at time t is given as

$$\varepsilon(t) = F_{m,p}^{(t)}[x_{m,p}(t)] \qquad \text{(Equation 4)}$$

$x_{m,p}(t)$ is the climate model value m within the projection period p, and $F_{m,p}^{(t)}$ is the time-dependent cumulative distribution function (CDF) of the climate model projection $x_{m,p}$. Using a 30-year moving window, $x_{m,p}$ is calculated based on the empirical CDF. $F_{m,c}^{[t-1]}$ is the simulations' inverse CDF during the calibration periods.

The model's ε quantile is bias corrected from observations across the calibration period:

$$\widehat{x}(t) = F_{o,c}^{[t-1]}[\varepsilon(t)] \qquad \text{(Equation 5)}$$

where $\widehat{x}$ is the bias-corrected quantile.

The inverse CDF during the calibration period, $F_{o,c}^{[t-1]}$, is calculated from observation $x_{o,c}$.

The final bias-corrected model projection x_c at time t is given as

$$x_c(t) = \widehat{x}(t)\Delta(t), \text{for conservative variables} \qquad \text{(Equation 6)}$$

$$x_c(t) = \widehat{x}(t) + \Delta(t), \text{for non} - \text{conservative variables} \qquad \text{(Equation 7)}$$

The MBCN method incorporates a QDM approach to enhance the N-dimensional probability density function transformation method by leveraging information from the variables $X_{m,c}, X_{m,p}$ and $X_{o,c}$. These variables undergo a rotational transformation, and the absolute changes described in Equations 6 and 7 are applied to each rotated $X_{m,c}, X_{m,p}$, and $X_{o,c}$ variable. Subsequently, the rotated $X_{m,c}$, $X_{m,p}$, and $X_{o,c}$ are transformed to $X_{m,c}^{[t+1]}, X_{m,p}^{[t+1]}$, and $X_{o,c}^{[t+1]}$. This iterative process continues until $X_{m,c}^{[t+1]}$ converges to $X_{o,c}$. Additionally, the ordinal rankings of each column in $X_{m,p}$ are adjusted to align with the ordinal rankings of the corresponding elements in each column of $X_{m,p}^{[t+1]}$.

Performance statistics for GCMs

The performance of BC methods and GCMs is based on seasonal, monthly, and annual timescales and is investigated using the MedAE, RMSE–observation standard deviation ratio (RSR),[20] RAE, and RMSE.

RSR

RSR is the ratio of the RMSE between the reference and model output and the reference standard deviation.[20,88] This is given as

$$RSR = \frac{RMSE}{SD_{reference}} = \frac{\sqrt{\sum_{i=1}^{n}\left[Y_i^{reference} - Y_i^{model}\right]^2}}{\sqrt{\sum_{i=1}^{n}\left[Y_i^{reference} - Y^{mean}\right]^2}} \qquad \text{(Equation 8)}$$

RSR ranges from 0, which denotes zero residual variation or RMSE, indicating an accurate model simulation, to a significant positive number, suggesting an imperfect model.

MedAE

The MedAE resists outliers.

Given that $\widehat{y}$ is the model output of the i_{th} sample, and y_i is the reference, MedAE estimated over N samples is defined as

$$MedAE(y, \widehat{y}) = median(|y_i - \widehat{y}_1|, ..., |y_n - \widehat{y}_n|) \qquad \text{(Equation 9)}$$

RAE

The RAE normalizes the total absolute error by dividing it by the total absolute error of the predictor. The resulting RAE index can range from 0 to infinity, where 0 indicates the ideal scenario:

$$RAE_v = \frac{\sum_{u=1}^{n}|model_{vu} - reference_u|}{\sum_{u=1}^{n}\left|reference_u - \frac{1}{n}\sum_{u=1}^{n}reference_u\right|} \qquad \text{(Equation 10)}$$

where $model_{vu}$ is the value predicted by individual model v for record u out of n records, and $reference_u$ is the reference value for record u.

Trends and dependency structure

WS variables are subjected to the modified Mann-Kendall (MMK) trend test,[31,34,50,89] while Sen's estimator[9,23,33,90] is used to estimate the magnitude of the trends. Also, a 30-year multiple-period trend[50] is used to examine the

trends over different timescales. This method depicts trends throughout various timescales, considering each trend's unique characteristics from its inception to its conclusion.[50] The joint dependency structures are estimated from the RMSE of the correlation coefficients between WS and other water budget variables.[33]

Self-organizing maps and WS classifications

The SOM, an artificial neural network technique, organizes training data input space into a two-dimensional discrete grid.[31] One neuron in the grid is assigned to each chunk of data, and the distance between neurons indicates how similar the chunks are.[46] Based on the distribution of the weight vectors, the SOM method groups the training datasets into a two-dimensional grid representing several clusters. After that, SOM partitions into clusters by taking data samples from each stratum. As a result, the datasets with equal variance and bias are grouped as one.[31,46] We employ the partitioning around medoids (PAM) algorithm[91] to determine the optimal clustering classification in the reduced feature space, guided by the gap statistics.[92,93] With the gap statistic, the total within-cluster variance[94] is compared with what would be predicted by a reference null distribution for various values of *k* (the number of clusters). The gap statistics' maximum value, which indicates that the data have been well clustered and that the clusters are well separated, is the ideal *k*. Utilizing the gap statistics prevents the data from being over- or underfitted.

Additionally, we employ the expectation maximization algorithms of Gaussian mixture models (GMM)[31] with different covariance structures[95] for parameter estimation of the SOM nodes, while the spatially explicit priors[96] maintain the spatial heterogeneity to validate the PAM-generated clusters. This approach facilitates the organization of SOM nodes into distinct groups. We select the best GMM using the Bayesian Information Criterion (BIC).[31] Therefore, we adopt the GMM with the lowest BIC value for clustering the SOM nodes. Leveraging the SOM and GMM, we generate 11 WS classification units. More information regarding the interface between SOM and GMM can be found in Adeyeri et al.[31]

LULC classification

Land Cover Type v.6 of the MODIS (MCD12Q1) categorizes land cover based on distinct thematic categories.[97] The International Geosphere-Biosphere Program (IGBP) type 1 land cover scheme identifies 17 land cover categories comprising 11 classes of natural vegetation, three classes of developed and mosaicked land, and three classes of non-vegetated land. We reclassify the IGBP land cover classes into 12 distinct classes (Figure 5) based on interval similarity.[31,98] Reclassification through interval similarity entails grouping data into intervals and assigning a consistent new value to all data points within each interval. This approach merges comparable land use types during land use reclassifications, streamlining data analysis, and simplifying interpretation.

Atmospheric river dynamics

We adopt the vertically integrated vapor transport (IVT) to understand the dynamics of water vapor movement in or out of a particular domain. IVT is defined as

$$IVT = \frac{1}{g} \int_{ptop = 300hPa}^{psurface = 1000hPa} q \vec{V} dp \qquad \text{(Equation 11)}$$

where *g* is the gravitational constant, $\vec{V}$ is the horizontal wind vector, *q* is the specific humidity, *psurface* is the pressure at the surface, and *ptop* is the pressure at the top of the atmosphere.

SUPPLEMENTAL INFORMATION

Supplemental information can be found online at https://doi.org/10.1016/j.oneear.2023.12.013.

AUTHOR CONTRIBUTIONS

O.E.A., conceptualization, software, resources, data curation, methodology, scripting, investigation, formal analysis, visualization, writing – original draft, review, and validation; W.Z., review, supervision, validation, funding acquisition, resources, and project administration; C.E.N., validation, review, and editing; X.W., supervision; K.A.I., validation, writing – review, editing; P.L., review and editing.

DECLARATION OF INTERESTS

The authors declare no competing interests.

REFERENCES

1. Xu, F., Zhao, L., Jia, Y., Niu, C., Liu, X., and Liu, H. (2022). Evaluation of water conservation function of Beijiang River basin in Nanling Mountains, China, based on WEP-L model. Ecol. Indicat. *134*, 108383.

2. Zhang, X., Li, J., Wang, Z., and Dong, Q. (2022). Global hydroclimatic drivers of terrestrial water storage changes in different climates. Catena *219*, 106598.

3. Li, M., Liang, D., Xia, J., Song, J., Cheng, D., Wu, J., Cao, Y., Sun, H., and Li, Q. (2021). Evaluation of water conservation function of Danjiang River Basin in Qinling Mountains, China based on InVEST model. J. Environ. Manag. *286*, 112212.

4. Adeyeri, O.E., Zhou, W., Laux, P., Ndehedehe, C.E., Wang, X., Usman, M., and Akinsanola, A.A. (2023). Multivariate Drought Monitoring, Propagation, and Projection Using Bias-Corrected General Circulation Models. Earth's Future *11*.

5. Postel, S.L., Daily, G.C., and Ehrlich, P.R. (1996). Human Appropriation of Renewable Fresh Water. Science *271*, 785–788.

6. Adeyeri, O.E., Zhou, W., Laux, P., Wang, X., Dieng, D., Widana, L.A., and Usman, M. (2023). Land use and land cover dynamics: Implications for thermal stress and energy demands. Renew. Sustain. Energy Rev. *179*, 113274.

7. Condon, L.E., Atchley, A.L., and Maxwell, R.M. (2020). Evapotranspiration depletes groundwater under warming over the contiguous United States. Nat. Commun. *11*, 873.

8. Ukkola, A.M., and Prentice, I.C. (2013). A worldwide analysis of trends in water-balance evapotranspiration. Hydrol. Earth Syst. Sci. *17*, 4177–4187.

9. Adeyeri, O.E., and Ishola, K.A. (2021). Variability and Trends of Actual Evapotranspiration over West Africa: The Role of Environmental Drivers. Agric. For. Meteorol. *308–309*, 108574.

10. Kurkute, S., Li, Z., Li, Y., and Huo, F. (2020). Assessment and projection of the water budget over western Canada using convection-permitting weather research and forecasting simulations. Hydrol. Earth Syst. Sci. *24*, 3677–3697.

11. Zhang, M., and Wei, X. (2021). Deforestation, forestation, and water supply. Science *371*, 990–991.

12. Tapley, B.D., Bettadpur, S., Watkins, M., and Reigber, C. (2004). The gravity recovery and climate experiment: Mission overview and early results. Geophys. Res. Lett. *31*.

13. Deng, S., Liu, S., and Mo, X. (2020). Assessment of Three Common Methods for Estimating Terrestrial Water Storage Change with Three Reanalysis Datasets. J. Clim. *33*, 511–525.

14. Rodell, M., Famiglietti, J.S., Wiese, D.N., Reager, J.T., Beaudoing, H.K., Landerer, F.W., and Lo, M.-H. (2018). Emerging trends in global freshwater availability. Nature *557*, 651–659.

15. Yang, P., Xia, J., Zhan, C., Qiao, Y., and Wang, Y. (2017). Monitoring the spatio-temporal changes of terrestrial water storage using GRACE data in the Tarim River basin between 2002 and 2015. Sci. Total Environ. *595*, 218–228.

16. Lehmann, F., Vishwakarma, B.D., and Bamber, J. (2021). How Well Are We Able to Close the Water Budget at the Global Scale?.

17. Ndehedehe, C., Awange, J., Agutu, N., Kuhn, M., and Heck, B. (2016). Understanding changes in terrestrial water storage over West Africa between 2002 and 2014. Adv. Water Resour. *88*, 211–230.

18. Yang, X., Tian, S., Feng, W., Ran, J., You, W., Jiang, Z., and Gong, X. (2020). Spatio-Temporal Evaluation of Water Storage Trends from Hydrological Models over Australia Using GRACE Mascon Solutions. Rem. Sens. *12*, 3578.

19. Deng, S., Liu, Y., and Zhang, W. (2023). A Comprehensive Evaluation of GRACE-Like Terrestrial Water Storage (TWS) Reconstruction Products at an Interannual Scale During 1981–2019. Water Resour. Res. *59*.

20. Adeyeri, O.E., Laux, P., Arnault, J., Lawin, A.E., and Kunstmann, H. (2020). Conceptual hydrological model calibration using multi-objective optimization techniques over the transboundary Komadugu-Yobe basin, Lake Chad Area, West Africa. J. Hydrol.: Reg. Stud. *27*, 100655.

21. Oliveira, P.T.S., Nearing, M.A., Moran, M.S., Goodrich, D.C., Wendland, E., and Gupta, H.V. (2014). Trends in water balance components across the Brazilian Cerrado. Water Resour. Res. *50*, 7100–7114.

22. Saemian, P., Elmi, O., Vishwakarma, B.D., Tourian, M.J., and Sneeuw, N. (2020). Analyzing the Lake Urmia restoration progress using ground-based and spaceborne observations. Sci. Total Environ. *739*, 139857.

23. Adeyeri, O.E., Laux, P., Lawin, A.E., Ige, S.O., and Kunstmann, H. (2020). Analysis of hydrometeorological variables over the transboundary Komadugu-Yobe basin, West Africa. J. Water Clim. Chang. *11*, 1339–1354.

24. Bhattarai, N., Mallick, K., Stuart, J., Vishwakarma, B.D., Niraula, R., Sen, S., and Jain, M. (2019). An automated multi-model evapotranspiration mapping framework using remotely sensed and reanalysis data. Rem. Sens. Environ. *229*, 69–92.

25. Wan, Z., Zhang, K., Xue, X., Hong, Z., Hong, Y., and Gourley, J.J. (2015). Water balance-based actual evapotranspiration reconstruction from ground and satellite observations over the conterminous United States. Water Resour. Res. *51*, 6485–6499.

26. Ndehedehe, C.E., Adeyeri, O.E., Onojeghuo, A.O., Ferreira, V.G., Kalu, I., and Okwuashi, O. (2023). Understanding global groundwater-climate interactions. Sci. Total Environ. *904*, 166571.

27. Adeyeri, O.E., Laux, P., Lawin, A.E., and Arnault, J. (2020). Assessing the impact of human activities and rainfall variability on the river discharge of Komadugu-Yobe Basin, Lake Chad Area. Environ. Earth Sci. *79*, 143.

28. An, L., Wang, J., Huang, J., Pokhrel, Y., Hugonnet, R., Wada, Y., Cáceres, D., Müller Schmied, H., Song, C., Berthier, E., et al. (2021). Divergent Causes of Terrestrial Water Storage Decline Between Drylands and Humid Regions Globally. Geophys. Res. Lett. *48*.

29. Jia, Y., Zhao, H., Niu, C., Jiang, Y., Gan, H., Xing, Z., Zhao, X., and Zhao, Z. (2009). A WebGIS-based system for rainfall-runoff prediction and real-time water resources assessment for Beijing. Comput. Geosci. *35*, 1517–1528.

30. Adeyeri, O.E., Akinsanola, A.A., and Ishola, K.A. (2017). Investigating surface urban heat island characteristics over Abuja, Nigeria: Relationship between land surface temperature and multiple vegetation indices. Remote Sens. Appl.: Society and Environment *7*, 57–68.

31. Adeyeri, O.E., Folorunsho, A.H., Ayegbusi, K.I., Bobde, V., Adeliyi, T.E., Ndehedehe, C.E., and Akinsanola, A.A. (2024). Land surface dynamics and meteorological forcings modulate land surface temperature characteristics. Sustain. Cities Soc. *101*, 105072.

32. Xu, L., Chen, N., Zhang, X., and Chen, Z. (2019). Spatiotemporal Changes in China's Terrestrial Water Storage From GRACE Satellites and Its Possible Drivers. JGR. Atmospheres *124*, 11976–11993.

33. Adeyeri, O.E., Laux, P., Lawin, A.E., and Oyekan, K.S.A. (2020). Multiple bias-correction of dynamically downscaled CMIP5 climate models temperature projection: a case study of the transboundary Komadugu-Yobe river basin, Lake Chad region, West Africa. SN Appl. Sci. *2*, 1221.

34. Adeyeri, O.E., Zhou, W., Wang, X., Zhang, R., Laux, P., Ishola, K.A., and Usman, M. (2022). The trend and spatial spread of multisectoral climate extremes in CMIP6 models. Sci. Rep. *12*, 21000.

35. Dieng, D., Cannon, A.J., Laux, P., Hald, C., Adeyeri, O., Rahimi, J., Srivastava, A.K., Mbaye, M.L., and Kunstmann, H. (2022). Multivariate Bias-Correction of High-Resolution Regional Climate Change Simulations for West Africa: Performance and Climate Change Implications. JGR. Atmospheres *127*.

36. Rasmussen, R., Liu, C., Ikeda, K., Gochis, D., Yates, D., Chen, F., Tewari, M., Barlage, M., Dudhia, J., Yu, W., et al. (2011). High-Resolution Coupled Climate Runoff Simulations of Seasonal Snowfall over Colorado: A Process Study of Current and Warmer Climate. J. Clim. *24*, 3015–3048.

37. Laux, P., Rötter, R.P., Webber, H., Dieng, D., Rahimi, J., Wei, J., Faye, B., Srivastava, A.K., Bliefernicht, J., Adeyeri, O., et al. (2021). To bias correct or not to bias correct? An agricultural impact modelers' perspective on regional climate model data. Agric. For. Meteorol. *304–305*, 108406.

38. Pascolini-Campbell, M.A., Reager, J.T., and Fisher, J.B. (2020). GRACE-based Mass Conservation as a Validation Target for Basin-Scale Evapotranspiration in the Contiguous United States. Water Resour. Res. *56*.

39. Swann, A.L.S., and Koven, C.D. (2017). A Direct Estimate of the Seasonal Cycle of Evapotranspiration over the Amazon Basin. J. Hydrometeorol. *18*, 2173–2185.

40. Wong, J.S., Zhang, X., Gharari, S., Shrestha, R.R., Wheater, H.S., and Famiglietti, J.S. (2021). Assessing Water Balance Closure Using Multiple Data Assimilation and Remote Sensing-Based Datasets for Canada. J. Hydrometeorol. *22*, 1569–1589.

41. Xiong, J., Guo, S., Chen, J., and Yin, J. (2022). Global evaluation of the "dry gets drier, and wet gets wetter" paradigm from a terrestrial water storage change perspective. Hydrol. Earth Syst. Sci. *26*, 6457–6476.

42. Cannon, A.J. (2016). Multivariate Bias Correction of Climate Model Output: Matching Marginal Distributions and Intervariable Dependence Structure. J. Clim. *29*, 7045–7064.

43. Cannon, A.J. (2018). Multivariate quantile mapping bias correction: an N-dimensional probability density function transform for climate model simulations of multiple variables. Clim. Dynam. *50*, 31–49.

44. Mehrotra, R., and Sharma, A. (2016). A Multivariate Quantile-Matching Bias Correction Approach with Auto- and Cross-Dependence across Multiple Time Scales: Implications for Downscaling. J. Clim. *29*, 3519–3539.

45. Rocheta, E., Evans, J.P., and Sharma, A. (2014). Assessing atmospheric bias correction for dynamical consistency using potential vorticity. Environ. Res. Lett. *9*, 124010.

46. Kohonen, T. (2013). Essentials of the self-organizing map. Neural Network. *37*, 52–65.

47. Di Virgilio, G., Ji, F., Tam, E., Nishant, N., Evans, J.P., Thomas, C., Riley, M.L., Beyer, K., Grose, M.R., Narsey, S., and Delage, F. (2022). Selecting CMIP6 GCMs for CORDEX Dynamical Downscaling: Model Performance, Independence, and Climate Change Signals. Earth's Future *10*.

48. Box, J.E., Cressie, N., Bromwich, D.H., Jung, J.-H., van den Broeke, M., van Angelen, J.H., Forster, R.R., Miège, C., Mosley-Thompson, E., Vinther, B., and McConnell, J.R. (2013). Greenland Ice Sheet Mass Balance Reconstruction. Part I: Net Snow Accumulation (1600–2009). J. Clim. *26*, 3919–3934.

49. Xiong, J., Guo, S., Yin, J., Ning, Z., Zeng, Z., and Wang, R. (2022). Projected changes in terrestrial water storage and associated flood potential across the Yangtze River basin. Sci. Total Environ. *817*, 152998.

50. Adeyeri, O.E., Laux, P., Ishola, K.A., Zhou, W., Balogun, I.A., Adeyewa, Z.D., and Kunstmann, H. (2022). Homogenizing meteorological variables: Impact on trends and associated climate indices. J. Hydrol. *607*, 127585.

51. Bevacqua, E., Suarez-Gutierrez, L., Jézéquel, A., Lehner, F., Vrac, M., Yiou, P., and Zscheischler, J. (2023). Advancing research on compound weather and climate events via large ensemble model simulations. Nat. Commun. *14*, 2145.

52. Ahmed, N., Lü, H., Ahmed, S., Adeyeri, O.E., Ali, S., Hussain, R., and Shah, S. (2023). Transboundary River Water Availability to Ravi Riverfront under Changing Climate: A Step towards Sustainable Development. Sustainability *15*, 3526.

53. Berg, P., Haerter, J.O., Thejll, P., Piani, C., Hagemann, S., and Christensen, J.H. (2009). Seasonal characteristics of the relationship between daily precipitation intensity and surface temperature. J. Geophys. Res. *114*.

54. Liu, Y., Jiang, Q., Wang, Q., Jin, Y., Yue, Q., Yu, J., Zheng, Y., Jiang, W., and Yao, X. (2022). The divergence between potential and actual evapotranspiration: An insight from climate, water, and vegetation change. Sci. Total Environ. *807*, 150648.

55. Cannon, A.J., Sobie, S.R., and Murdock, T.Q. (2015). Bias Correction of GCM Precipitation by Quantile Mapping: How Well Do Methods Preserve Changes in Quantiles and Extremes? J. Clim. *28*, 6938–6959.

56. Farrick, K.K., and Branfireun, B.A. (2014). Soil water storage, rainfall and runoff relationships in a tropical dry forest catchment. Water Resour. Res. *50*, 9236–9250.

57. Penna, D., Tromp-van Meerveld, H.J., Gobbi, A., Borga, M., and Dalla Fontana, G. (2011). The influence of soil moisture on threshold runoff generation processes in an alpine headwater catchment. Hydrol. Earth Syst. Sci. *15*, 689–702.

58. Descroix, L., Guichard, F., Grippa, M., Lambert, L., Panthou, G., Mahé, G., Gal, L., Dardel, C., Quantin, G., Kergoat, L., et al. (2018). Evolution of Surface Hydrology in the Sahelo-Sudanian Strip: An Updated Review. Water *10*, 748.

59. Brandt, M., Rasmussen, K., Hiernaux, P., Herrmann, S., Tucker, C.J., Tong, X., Tian, F., Mertz, O., Kergoat, L., Mbow, C., et al. (2018). Reduction of tree cover in West African woodlands and promotion in semi-arid farmlands. Nat. Geosci. *11*, 328–333.

60. Nicholson, S.E. (2001). Climatic and environmental change in Africa during the last two centuries. Clim. Res. *17*, 123–144.

61. Vizy, E.K., Cook, K.H., Crétat, J., and Neupane, N. (2013). Projections of a Wetter Sahel in the Twenty-First Century from Global and Regional Models. J. Clim. *26*, 4664–4687.

62. Sheen, K.L., Smith, D.M., Dunstone, N.J., Eade, R., Rowell, D.P., and Vellinga, M. (2017). Skilful prediction of Sahel summer rainfall on interannual and multi-year timescales. Nat. Commun. *8*, 14966.

63. Piaggio, M., and Siikamäki, J. (2021). The value of forest water purification ecosystem services in Costa Rica. Sci. Total Environ. *789*, 147952.

64. Kasurinen, V., Alfredsen, K., Kolari, P., Mammarella, I., Alekseychik, P., Rinne, J., Vesala, T., Bernier, P., Boike, J., Langer, M., et al. (2014). Latent heat exchange in the boreal and arctic biomes. Global Change Biol. *20*, 3439–3456.

65. Nicholls, E.M., and Carey, S.K. (2021). Evapotranspiration and energy partitioning across a forest-shrub vegetation gradient in a subarctic, alpine catchment. J. Hydrol. *602*, 126790.

66. Lélé, M.I., and Leslie, L.M. (2016). Intraseasonal variability of low-level moisture transport over West Africa. Clim. Dynam. *47*, 3575–3591.

67. Cook, K.H. (1999). Generation of the African Easterly Jet and Its Role in Determining West African Precipitation. J. Clim. *12*, 1165–1184.

68. Zhuo, L., and Zhou, L. (2022). Moisture transport and water vapour budget over the Sahara Desert. Int. J. Climatol. *42*, 6829–6843.

69. Liu, W., Cook, K.H., and Vizy, E.K. (2020). Role of the West African westerly jet in the seasonal and diurnal cycles of precipitation over West Africa. Clim. Dynam. *54*, 843–861.

70. Trenberth, K.E., Fasullo, J.T., and Kiehl, J. (2009). Earth's Global Energy Budget. Bull. Am. Meteorol. Soc. *90*, 311–324.

71. Algarra, I., Nieto, R., Ramos, A.M., Eiras-Barca, J., Trigo, R.M., and Gimeno, L. (2020). Significant increase of global anomalous moisture uptake feeding landfalling Atmospheric Rivers. Nat. Commun. *11*, 5082.

72. Evan, A.T., Flamant, C., Lavaysse, C., Kocha, C., and Saci, A. (2015). Water Vapor–Forced Greenhouse Warming over the Sahara Desert and the Recent Recovery from the Sahelian Drought. J. Clim. *28*, 108–123.

73. Ranjha, R., Svensson, G., Tjernström, M., and Semedo, A. (2013). Global distribution and seasonal variability of coastal low-level jets derived from ERA-Interim reanalysis. Tellus Dyn. Meteorol. Oceanogr. *65*, 20412.

74. Zhang, Y., Liu, K., Li, Y., Shen, W., Ren, Y., Zeng, D., and Sha, S. (2021). Water Vapor Changes Affect Cross-Seasonal Strong Drought Events in the Eastern Region of Northwest China. Front. Earth Sci. *9*.

75. Ramos, A.M., Trigo, R.M., Liberato, M.L.R., and Tomé, R. (2015). Daily Precipitation Extreme Events in the Iberian Peninsula and Its Association with Atmospheric Rivers. J. Hydrometeorol. *16*, 579–597.

76. Adeyeri, O.E. (2023). Minimizing Uncertainties in Climate Projections Reveals the Vulnerability of Terrestrial Water Storage to Climate Change.

77. O'Neill, B.C., Tebaldi, C., van Vuuren, D.P., Eyring, V., Friedlingstein, P., Hurtt, G., Knutti, R., Kriegler, E., Lamarque, J.-F., Lowe, J., et al. (2016). The Scenario Model Intercomparison Project (ScenarioMIP) for CMIP6. Geosci. Model Dev *9*, 3461–3482.

78. Harris, I., Osborn, T.J., Jones, P., and Lister, D. (2020). Version 4 of the CRU TS monthly high-resolution gridded multivariate climate dataset. Sci. Data *7*, 109.

79. Ghiggi, G., Humphrey, V., Seneviratne, S.I., and Gudmundsson, L. (2021). G-RUN ENSEMBLE: A Multi-Forcing Observation-Based Global Runoff Reanalysis. Water Resour. Res. *57*.

80. KOBAYASHI, S., OTA, Y., HARADA, Y., EBITA, A., MORIYA, M., ONODA, H., ONOGI, K., KAMAHORI, H., KOBAYASHI, C., ENDO, H., et al. (2015). The JRA-55 Reanalysis: General Specifications and Basic Characteristics. J. Meteorol. Soc. Jpn. *93*, 5–48.

81. Ndehedehe, C.E., Ferreira, V.G., Adeyeri, O.E., Correa, F.M., Usman, M., Oussou, F.E., Kalu, I., Okwuashi, O., Onojeghuo, A.O., Getirana, A., and Dewan, A. (2023). Global assessment of drought characteristics in the Anthropocene. Resources, Environment and Sustainability *12*, 100105.

82. Schulzweida, U. (2022). CDO User Guide (Zenodo).

83. Humphrey, V., and Gudmundsson, L. (2019). GRACE-REC: a reconstruction of climate-driven water storage changes over the last century. Earth Syst. Sci. Data *11*, 1153–1170.

84. Humphrey, V., and Gudmundsson, L. (2019). GRACE-REC: A reconstruction of climate-driven water storage changes over the last century (figshare).

85. Adeyeri, O.E., Lawin, A.E., Laux, P., Ishola, K.A., and Ige, S.O. (2019). Analysis of climate extreme indices over the Komadugu-Yobe basin, Lake Chad region: Past and future occurrences. Weather Clim. Extrem. *23*, 100194.

86. Déqué, M., Rowell, D.P., Lüthi, D., Giorgi, F., Christensen, J.H., Rockel, B., Jacob, D., Kjellström, E., de Castro, M., and van den Hurk, B. (2007). An intercomparison of regional climate simulations for Europe: assessing uncertainties in model projections. Climatic Change *81*, 53–70.

87. Piani, C., Haerter, J.O., and Coppola, E. (2010). Statistical bias correction for daily precipitation in regional climate models over Europe. Theor. Appl. Climatol. *99*, 187–192.

88. Moriasi, D.N., Arnold, J.G., van Liew, M.W., Bingner, R.L., Harmel, R.D., and Veith, T.L. (2007). Model Evaluation Guidelines for Systematic Quantification of Accuracy in Watershed Simulations. Trans. ASABE (Am. Soc. Agric. Biol. Eng.) *50*, 885–900.

89. Oyerinde, G.T., Lawin, A.E., and Adeyeri, O.E. (2021). Multi-variate infilling of missing daily discharge data on the Niger basin. Water Pract. Technol. *16*, 961–979.

90. Sen, P.K. (1968). Estimates of the Regression Coefficient Based on Kendall's Tau. J. Am. Stat. Assoc. *63*, 1379–1389.

91. Kaufman, L., and Rousseeuw, P.J. (2008). Finding Groups in Data. An Introduction to Cluster Analysis (John Wiley & Sons).

92. Dudoit, S., and Fridlyand, J. (2002). A prediction-based resampling method for estimating the number of clusters in a dataset. Genome Biol. *3*. RESEARCH0036.

93. Tibshirani, R., Walther, G., and Hastie, T. (2001). Estimating the number of data clusters via the Gap statistic. J. Roy. Stat. Soc. B *63*, 411–423.

94. Callahan, C.W., and Mankin, J.S. (2020). The Influence of Internal Climate Variability on Projections of Synoptically Driven Beijing Haze. Geophys. Res. Lett. *47*.

95. Scrucca, L., Fop, M., Murphy, T., and Raftery, A.E. (2016). mclust 5: Clustering, Classification and Density Estimation Using Gaussian Finite Mixture Models. R J. *8*, 289–317.

96. Crandall, D., Felzenszwalb, P., and Huttenlocher, D. (2005). Spatial Priors for Part-Based Recognition Using Statistical Models. In Los Alamitos, Calif., C.S. Proceedings, ed. (IEEE Computer Society)), pp. 10–17.

97. Friedl, M., and Sulla-Menashe, D. (2022). MODIS/Terra+Aqua Land Cover Type Yearly L3 Global 500m SIN Grid V061 (NASA EOSDIS Land Processes DAAC).

98. Lillesand, T. (2015). Remote Sensing and Image Interpretation, 7th Edition (John Wiley & Sons, Incorporated).